Thermo-migration of moisture in Norway spruce assessed by in-situ micro-tomography

Benoît Martin, Julien Colin, Joel Casalinho, Patrick Perré, Romain Rémond

Thermo-migration of moisture in Norway spruce assessed by *in-situ* micro-tomography

Benoît Martin[1, 2*], *Julien* Colin[2, 3], *Joel* Casalinho[3], *Patrick* Perré[2, 3], *Romain* Rémond[1]

[1]LERMAB, Université de Lorraine, ENSTIB, Epinal, France

[2]Université Paris-Saclay, CentraleSupélec, Laboratoire de Génie des Procédés et Matériaux, Centre Européen de Biotechnologie et de Bioéconomie (CEBB), 3 rue des Rouges Terres 51110 Pomacle, France

[3]Université Paris-Saclay, CentraleSupélec, Laboratoire de Génie des Procédés et Matériaux, 8-10 rue Joliot Curie 91190 Gif-sur-Yvette, France

Abstract: Wood used as a building material is exposed to non-isothermal and unsteady state conditions involving coupled heat and mass transfer within the porous media. These exchanges contribute to the regulation of relative humidity in a passive way and influence the energy performance of buildings. In order to characterize the importance of the hygrothermal behaviour of softwoods in this context, an experimental setup was developed to access to moisture fluxes and/or moisture content profiles in the presence of a known temperature difference imposed on both sides of the wood sample. This original setup was conceived to maintain the temperature gap during micro-tomography acquisition. Image processing allows the moisture content profiles to be obtained over time after changes of the thermal gradient. The simulation using a computational model of coupled heat and mass transfer confirmed that the gradient of vapor density is a relevant unique, "synthetic", driving force to account for moisture migration in non-isothermal conditions.

Keywords: driving force, non-invasive method, simulation, thermal gradient, wood

1 Introduction

The hygroscopic equilibrium of solid wood is a function of the surrounding environmental conditions [1,2]. A change in temperature and ambient humidity leads to a new equilibrium resulting in a transfer of moisture within the material and at its boundaries. In the case of wooden buildings, temperature differences between the exterior and interior of the wall induce non-uniform profiles of equilibrium moisture content along the thickness. Therefore, non-isothermal conditions induce coupled heat and moisture transfers within the materials, that persist even at steady-state due to the exchanges at the boundaries. These exchanges participate in the regulation of the relative humidity of the interior rooms in a passive way and influence the energy performance of buildings, thanks to the latent heat of evaporation [3,4]. The monitoring of energy consumption at the whole building scale with its occupants is intended to allow comparison of experimental data with numerical models that estimate the hygrothermal performance of building materials [5,6]. However, the complexity of the real outdoor climate, the difficulty to quantify the air infiltration, the performance of ventilation system

and to characterize the impact of the occupants on the interior conditions makes it difficult to analyse the results [7]. To overcome these uncertainties, the study of the hygrothermal behaviour of buildings materials at the wall scale with a double climatic chamber is relevant [8–10]. The monitoring of thermal and mass transfer is obtained by inserting sensors (electrical capacitance or resistance) into the wall materials. The experimental data obtained are then compared with models simulating coupled heat and mass transfer in the porous media. The analysis of the results highlights the discrepancies that remain between the simulations and the experimental data, especially for bio-based materials where the heat-mass coupling is predominant [11,12]. In order to improve the predictive capacity of the models, the use of experimental data at the material scale is required.

Various works have been conducted to study moisture transfer in wood-based material under non-isothermal conditions to determine the moisture flux over the thickness of a sample [13–18]. To access moisture profiles within a wood sample exposed on one side to high temperature, 2D neutron imaging [19] and NMR [20] have been used. However, the thermal load was not representative to the daily thermal variations in building walls. To better understand moisture transfer in a wooden construction, the moisture fluxes and/or the moisture content profiles should be assessed in the presence of a known temperature difference imposed on both sides of the wood sample. This was done in [21] using a constant temperature difference of 20°C in a homogenous wood species. Their results suggested moisture content above the moisture saturation point on the cold side of the sample but the presence of liquid water could not be confirmed from the 2D X-ray images.

This study aims to use the potential of X-ray computed tomography imaging to access the moisture migration kinetics within a softwood sample (Norway Spruce), commonly used in wooden construction [22], subjected to realistic dynamic thermal loading. To meet the needs, an *in-situ* device was conceived and manufactured to set and maintain the desired temperature during CT imaging. This setup was used to follow the dynamic of moisture redistribution after a change of temperature on both sides of the sample. The imposed thermal solicitation sequence was intended to reproduce in a simplified way the real and usual conditions encountered in the building. During the sequence of thermal loads, different driving forces contributing to moisture diffusion (water vapor density gradient, moisture content gradient and thermal gradient) were present within the sample in the same or opposite directions.

X-ray imaging has the advantage to be a non-destructive and non-invasive method that does not disturb the local transfers. However, the establishment of variable temperatures on two opposite sides of the wood sample required the development of an original experimental setup. Its design meets the specificities of X-ray tomography and experimental needs as described in the following section. From

the CT images, several steps are required to obtain the evolution of moisture profiles within the sample, namely image processing and a calibration protocol to obtain the moisture content from the greyscale value of the CT. The non-isothermal moisture transfer within the sample is then discussed and analysed by using a computational model simulating the coupled heat and mass transfer in porous media.

2 Materials and methods

2.1 Materials and sample preparation

A cylindrical sample was cut from a Norway spruce (*Picea abies*) board extracted from a log harvested in the Auvergne region of France. The board with a total number of 73 annual rings counted from the pith to the bark was dried and stored in the laboratory since several years. The cylinder with a diameter of 20 mm and a length of 35 mm – in the radial direction – was machined with a 5-axis Computer Numerical Control (CNC) machine (SCM morbidelli 100). The sample was located at the annual rings 37 to 51. The sample was thus located in the heartwood of the tree.

To prevent any moisture exchange with the surrounding during the experiment, all surfaces of the sample were covered with a double layer of impermeable coating (Rubson, Liquid Rubber Plus). Thus, the average moisture content of the sample was kept at a constant value throughout the test. Only the moisture redistribution within the sample was observed with non-isothermal boundary conditions. A uniform application of the sealant was ensured by a miniature wood lathe specifically designed for this purpose. Rotation of the sample during the application and drying of the coating prevented gravity flow which would have resulted in an inhomogeneous distribution of the coating. Before applying each layer of coating, the surface was sanded with P320 abrasive paper to remove raised fibres, which eases the mechanical adhesion. Once the second layer of coating was dried, a flexible polyolefin shrink sleeve was added to complete the peripheral sealing. The sample was then cut to final length using a precision cutting machine (SECOTOM 50, Struers). Finally, a multi-layer sealing was applied on these two faces comprising a Rubson coating layer, an aluminium foil and again a Rubson coating layer.

The average moisture content of the sample was determined by double weighing a twin sample. Both samples were previously stored for six months in the same climate chamber (Memmert HPP110eco) set at a temperature of 25°C and a relative humidity of 87% to reach a relatively high moisture content equilibrium. At the end of this conditioning phase, the twin sample was weighed and then placed in an oven at 103°C to obtain its anhydrous mass. The moisture content, dry basis,

was determined at 17.5% and the dry density of the sample was calculated from its mass and dimensions at 415 $kg \cdot m^{-3}$.

2.2 X-ray computed tomography

2.2.1 Experimental setup

The design of the experimental setup was made to be compatible with X-ray tomography. It needed to meet several requirements and constraints:

- to set different temperature values, typical of buildings, on both opposite sides of a sample,
- to maintain the desired values during tomographic acquisitions, without vibration,
- to ensure a free sample rotation during acquisition,
- to record the actual temperature values over time,
- to limit heat transfer at the periphery of the sample.

The objective was to follow the dynamics of water redistribution after a temperature change on opposite sides of the sample according three phases of thermal loads (see section 2.2.2). As the moisture migration was slow, the duration of the experiments was significant (the data set for the present work represented three months of experimentation), requiring the tomograph to be freed up for other uses between two successive scans.

To meet these cumulative constraints, the device includes two independent temperature control systems positioned at each side of the sample (Figure 1). The mechanical connection of these two elements was provided by a polypropylene tube. The choice of this material was based on preliminary tests which proved that this material offers a lower X-ray attenuation than carbon and aluminium while having sufficient mechanical stiffness. A 3-mm thick layer of air between the polypropylene tube and the sample acts as thermal insulation.

The control of temperature at each opposite side of the sample was obtained by thermoelectric modules. Their operating principle is based on Peltier's effect: when an electric current passes through a module composed of two semiconductor materials of different nature, one side of the module releases heat and the other absorbs it. The phenomenon is reversed when the current is reversed. This solution had the double advantage of miniaturising the experimental device and facilitating the establishment of different temperatures. The power supply was ensured by batteries integrated into the assembly during the two-hour tomographic acquisition to maintain the temperatures without wires. Therefore, a complete rotation of the sample is allowed without vibration.

The desired temperature was controlled by an Arduino Nano microprocessor embedded in the regulation system. Operating in a closed loop, the algorithm – using an all or nothing power supply over a time base – regulates the current direction of the thermoelectric module by activating a dual relay module as a function of the temperature measured by a PT 1000 temperature sensor (Figure 1c). Direct visualisation of the proper operation of the control system was provided by a monitor displaying the set and measured temperatures on the opposite sides (top and bottom) of a sample. Once the acquisition was completed in the tomograph, the device was placed in a climatic chamber (T = 25°C) and connected to a computer for powering and data recording. A graphical interface – developed in the Visual Basic programming language – was developed to manually change the set temperature. This interface can also be used to change the type of power supply, i.e. a battery during tomographic acquisitions or the power grid when the device was in the climatic chamber. More detail is available in [23].

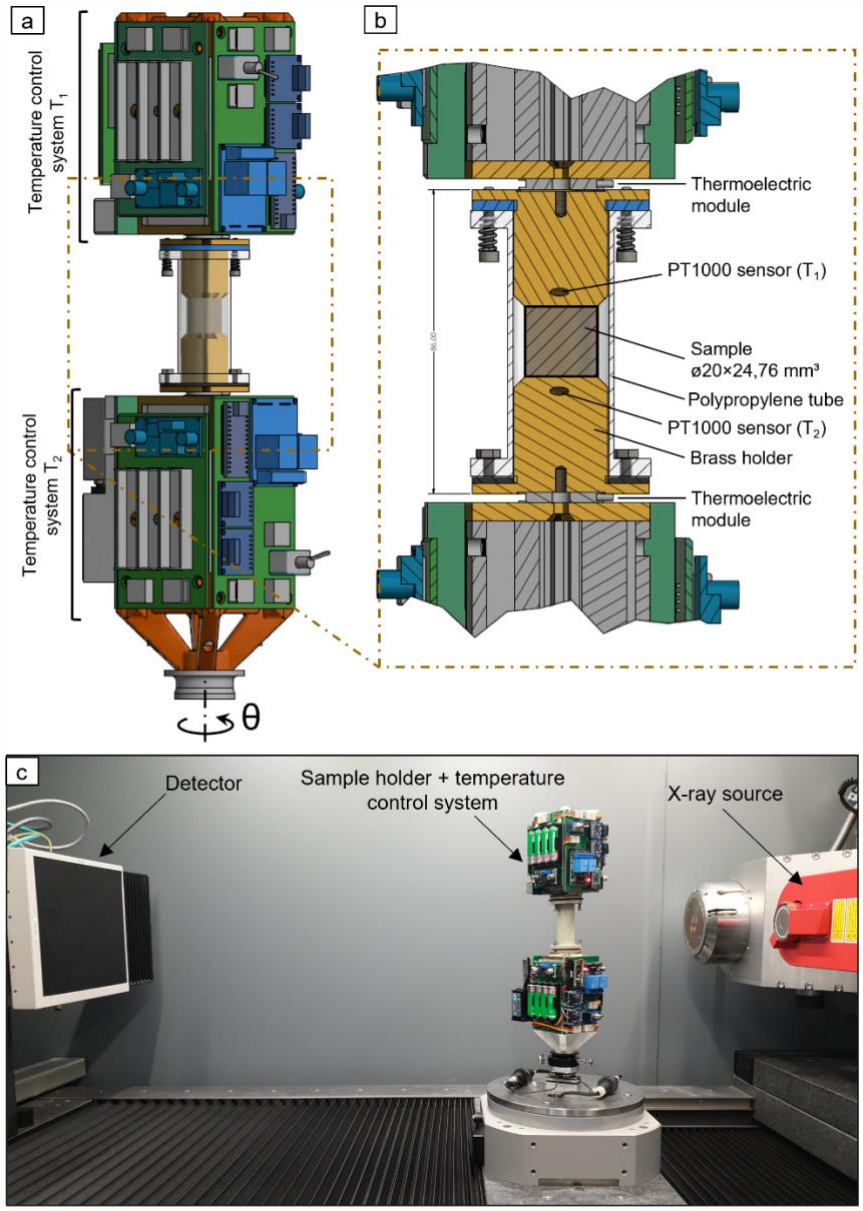

Figure 1: a) Design of the sample holder and instrumentation, b) Cross-sectional view and zoom on the sample and c) View of the device positioned in the X-ray tomograph

2.2.2 Time-evolution of boundary conditions

The sequence of thermal loads applied to both sides of the sample is depicted in Figure 2. After an initial state recorded at the equilibrium, the thermal sequence consisted of three phases with:

1) a constant temperature difference of 20°C applied on the opposite sides of the sample for 15 days to reproduce the stationary conditions encountered for example through a wall in winter (15°C at the top side and 35°C at the bottom side, Figure 1b),

2) a return to isothermal conditions with a temperature of 25°C on each side of the sample for 21 days,

3) temperature cycles of 15 and 35°C on one side (T_1, Figure 1b) and a constant temperature kept at 25°C on the opposite side (T_2, Figure 1b), to reproduce a dynamic behaviour observed for example in inter-season or summer (day-night cycles).

To follow moisture redistribution, the frequency of acquisitions was variable during the three months of the experiment. After a change in boundary conditions, two acquisitions were made on the following days and then the acquisition frequency decreased from once every two days to once a week (Figure 2).

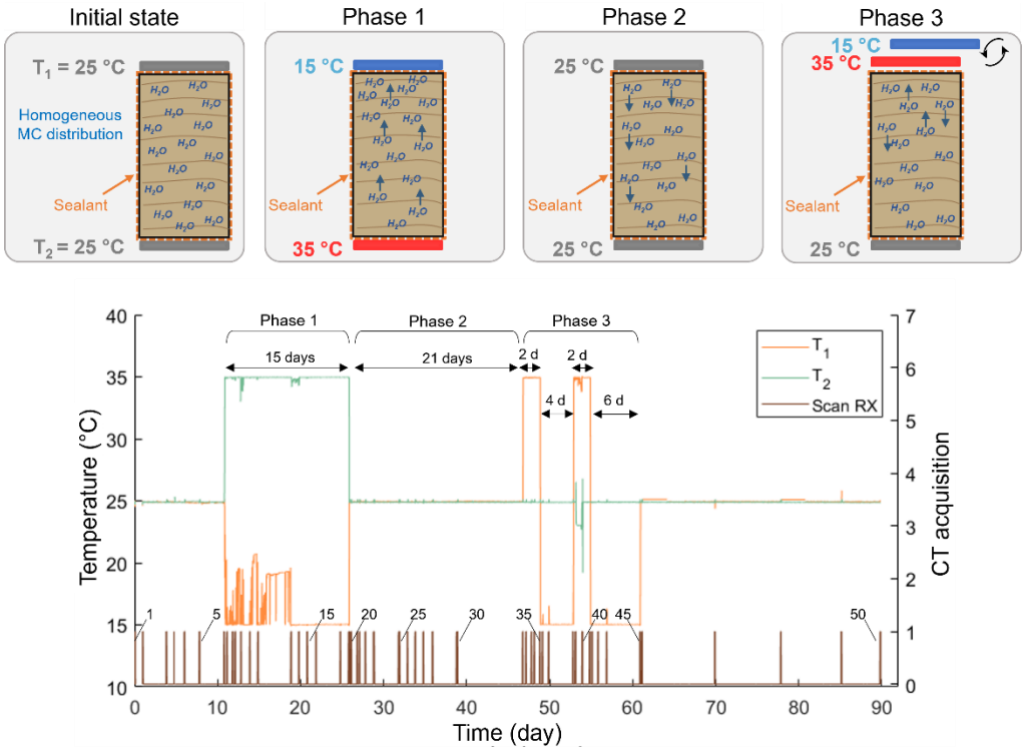

Figure 2: The sequence of temperature conditions imposed to the opposite sides of the sample (Figure 1b). The orange and green curves are the measured temperature and the frequency of CT acquisitions is shown by the brown lines.

2.2.3 Image acquisition and 3D numerical reconstructions

The acquisition of the 2D projections was carried out with a tomograph from RX Solutions (EasyTom XL Ultra 150-160). This versatile equipment features two X-ray source and two imagers. In order to fulfil the needs of the present work, the microfocus X-ray source and the detector were used according to the configuration described in Table 1 below:

Table 1: Acquisition parameters of X-ray source and detector

150 kV microfocus X-ray source	Detector
Voltage: 100 kV	Pixel size: 127 µm
Intensity: 210 µA	Exposure time: 0.5 s
Emission spot size: 20 µm	Number of averaged projections: 3

The source-detector distance was set at 1 m and the sample was placed at 0.34 m from the µX-ray generator, with a corresponding sample resolution of 40 µm. With these parameters, the recording time of the tomographic acquisition was about one hour for 1440 projections. Before, a calibration step of the acquisition chain – lasting several minutes – was intended to consider (i) the default values of the imager pixels and (ii) the heterogeneous distribution of the X-ray beam. Thus, two corrections were made with (i) the acquisition of a black field image corresponding to the grey level of the imager pixels recorded without X-ray emission, and (ii) a reference image without sample in the X-ray field to obtain the X-ray beam distribution on the imager. This reference image was recorded with the same parameters as those used during the acquisition of the projections. This calibration step was preceded by a necessary stabilisation step of the X-ray source after the whole support was set on the rotating stage. According to preliminary tests, a source stabilisation step of one hour was required after the X-ray generator was switched on. Therefore, in total, the sample and its active support were positioned in the tomograph for two hours.

After the scan, all projections are used in the reconstruction algorithm X-Act software provided by RX Solutions. This software used the classical back projection of CT scan, with suitable filters and a correction of the X-ray spot location. Once done, a discrete 3D image (40 µm-cubic voxels) of a cylinder parallel to the rotation axis is obtained (cubic voxels with size of 40 µm). This 3D information is provided as a stack of cross-sections of this cylinder along the z axis.

2.3 Moisture content determination

2.3.1 X-ray attenuation in relation to moisture content

Computed tomography is composed of two steps: the first one consists in recording a large number of 2D projections of the observed object under different angles during a complete rotation of the sample (360°). The second step is to perform the tomographic reconstruction – from the 2D projections – using the filtered back-projection method based on the Radon theorem [24,25]. The obtained greyscale value of the $CT_{numbers}$ reflects the ability of the material to attenuate X-rays. It is

a function of the chemical composition of the material, its density and the energy spectrum of the X-ray beam [26].

According to Lindgren (1992), wood density can be linked to the computed tomography number (CT_{number}), expressed in Hounsfield Units, using a linear relationship. This method has been used with success in several studies to estimate the density of various wood species [28–31]. The same relation can be used from the CT_{number} on the computed tomography image to the wood density (1).

$$\rho = A \cdot CT_{number} + B \quad (1)$$

with ρ the wood density (kg·m^{-3}), A and B constant values obtained by calibration.

In order to assess the moisture content measurement, it was assumed that the variations in density of water (changes in moisture content) and lignocellulosic material (shrinkage/swelling) had the same effect on the CT_{number}, in spite the small difference between cell wall and water [32,33]. This assumption allows a unique affine function to relate CT_{number} and moisture content:

$$\frac{\rho_0(i,j,k,t)}{1+\epsilon_v\big(X(i,j,k,t)\big)} \cdot \big(1 + X(i,j,k,t)\big) = A \cdot CT_{number}(i,j,k,t) + B \quad (2)$$

with ρ_0 the wood anhydrous density (kg·m^{-3}), ϵ_v the volume swelling compared to the anhydrous state and X the moisture content. The position of the pixel in the image being given by indices i, j, k (Cartesian reference). Parameters depending on time are defined at time *t.* The volume swelling could be expressed according to equation (3):

$$\epsilon_v\big(X(i,j,k,t)\big) = \frac{R_v}{1-R_v} \cdot \frac{X(i,j,k,t)}{X_{fsp}} \quad (3)$$

with R_v the total volume shrinkage of Norway spruce equal to 0.13 [34] and X_{fsp} the fibre saturation point equal to 0.29 [1].

The use of this linear relationship (equation (2) for the time evolution of the moisture content field requires three adjustments including two spatial and one temporal correction.

The first spatial correction is intended to overcome a reconstruction artifact related to the conicity of the X-ray beam, when the divergent X-rays pass through regions of different densities. This effect was visible in the air volume outside the polypropylene tube where horizontal lines were present while the CT_{number} was expected to be uniform. In order to remedy this reconstruction artifact, its relative impact was assumed uniform over a horizontal section of the reconstructed volume. The reduced $CT_{number}{}^{*}$ corresponding to the ratio between the CT_{number} of the point considered in the

wood (CT_{wood}) and the average CT_{number} of the air (CT_{air}) at the same height k has been introduced according to equation (4):

$$CT_{number}{}^{*}(i,j,k,t) = \frac{CT_{wood}(i,j,k,t)}{< CT_{air}(k,t) >} \quad (4)$$

Where $<CT_{air}>$ is the average value of $CT_{numbers}$ located outside the polypropylene tube at the same height in the reconstructed volume corresponding to the air.

In addition, by discretizing the horizontal section of the sample in the initial state into concentric zones, it was found that the $CT_{numbers}$ were not uniform. Whatever the height considered, the $CT_{numbers}$were higher in the centre of the sample than in the periphery, which indicates a bias of the reconstruction filter. For this reason, equation (2) was adapted by defining B as a function of the pixel distance from the axis of the sample (radius r, itself a function of the cartesian indices i and j):

$$\frac{\rho_0(i,j,k)}{1+\epsilon_v\big(X(i,j,k,t)\big)} \cdot \big(1 + X(i,j,k,t)\big) = A \cdot CT_{number}{}^{*}(i,j,k,t) + B\big(r(i,j)\big) \quad (5)$$

Finally, the last correction was intended to account for the temporal variations of the acquisition chain from one acquisition to another. This requires a known reference. In our case, the average moisture content of the sample at time *t* (*<X(t)>*) was used as a reference, as it remained constant during the test due to the multilayer waterproof coating on all sides of the sample. The temporal correction was performed to ensure that the average moisture content was always equal to the initial moisture content ($< X(t=0) >$), 17.5% here. The corrected moisture content could be then expressed according to equation (6):

$$X_{correct}(i,j,k,t) = X(i,j,k,t) \cdot \frac{< X(t=0) >}{< X(t) >} \quad (6)$$

In order to impose the criterion on the amount of water, the average moisture content should be based on the integration of the local moisture content weighted by the local anhydrous density:

$$< X(t) >= \frac{\sum_{i,j,k} X(i,j,k,t) \cdot \frac{\rho_0(i,j,k)}{1+\epsilon_v\big(X(i,j,k,t)\big)} \cdot V_{voxel}}{\sum_{i,j,k} \frac{\rho_0(i,j,k)}{1+\epsilon_v\big(X(i,j,k,t)\big)} \cdot V_{voxel}} \quad (7)$$

where V_{voxel} was the voxel volume.

2.3.2 Spatial discretization

The spatial distribution (radial, inter-ring and intra-ring) of water content was studied by discretising the sample into regions of interest (ROI). For this purpose, a MATLAB script was developed to automatically detect the contour of the sample according to the variation of the grey level caused by the Rubson coating. The sample section was divided into four homothetic cylinders named c_1, c_2, c_3 and c_4 (Figure 3a). Thus, the regions c_2 to c_4 were hollow cylinders. For each cylinder c_i, ROIs were defined along the height of the sample. Each annual ring was divided into three parts with: 45% of the ring height allocated to earlywood EW, 45% to transition wood (TW, between early and late wood) and 10% to latewood LW (Figure 3b and Figure 3c). These relative proportions were considered constant over the duration of the experiment. It should be noted that ring 38 – located at the end of the sample – was incomplete and therefore its real height was inaccessible. The determination of the boundary between transitional and latewood in this ring was defined according to the variation of the grey level. For this reason, the height of the area corresponding to latewood (#LW 38) was considered as constant without considering dimensional variations in the radial direction due to variations in bound water content. For ring 51 at the opposite end, the low height of the accessible ring made it impossible to distinguish the boundary between earlywood and transition wood. Therefore, a single ROI was defined between the ring boundary and this end of the sample. According to this method, the measured local density along the ring at the initial state for the cylinder c_1 is plotted in the Figure 4.

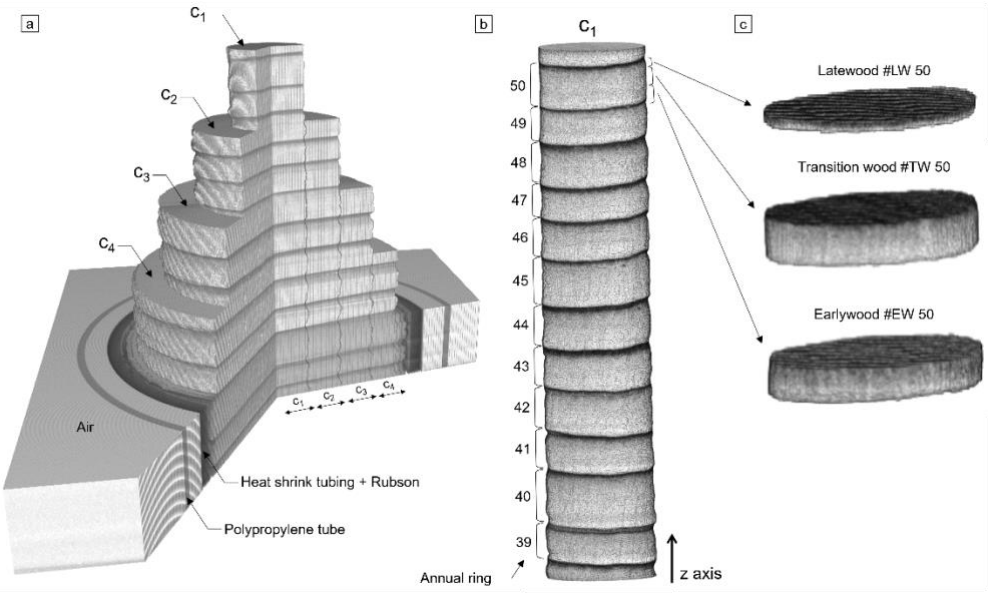

Figure 3: a) Axonometric view of the sample with cylinders c_1, c_2, c_3 and c_4, b) Zoom on the central cylinder c_1 and c) Example of the discretization of ring 50 into three regions of interest (ROI) with #LW 50, #TW 50 and #EW 50. The grey level has been inverted to facilitate visualisation. Thus, the dark grey levels denote the presence of denser material than a light grey level

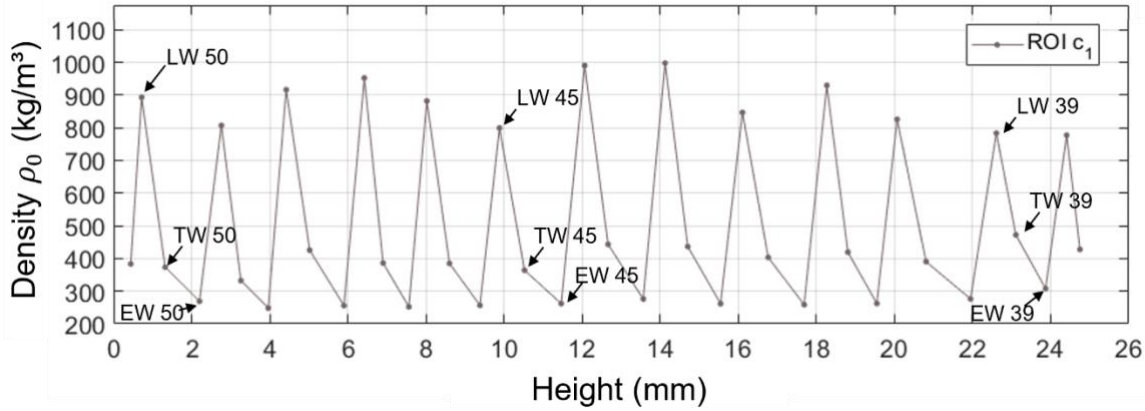

Figure 4: Wood density distribution by ROI along the height of the sample for the central cylinder c_1

This discretization enables equation (5) to be simplified, by considering average values of ρ_0, X and CT_{number} within each ROI and mean values of B for each cylinder c_i, with i = 1 to 4.

$$\frac{\rho_0(ROI)}{1+\epsilon_v\big(X(ROI,t)\big)}\cdot\big(1+X(ROI,t)\big)=A\cdot CT_{number}{}^{*}(ROI,t)+B(c_i) \quad (8)$$

A calibration procedure was defined to determine the values of A and B in equation 8 by using the initial state with a uniform moisture content throughout the sample. This procedure is detailed in appendix.

2.4 Numerical simulations

Simulations of the experimental configuration was performed using *TransPore*, a computational model of coupled heat and mass transfer in porous media [35–37]. The numerical simulation was carried out in 1D configuration, hence along the radial direction, the cylinder axis. The temperatures measured by the PT1000 sensors (Figure 2) were set as Dirichlet boundary conditions. The measured density profile of the sample is used as input data to the model, but the effect of density variation on the transfer properties such as capillary pressure, liquid permeability and diffusion coefficient, was not taken into account. It has be noted that the density profile locally modifies the porosity and thus the liquid saturation S_l, which affects the capillary pressure [38].

In *TransPore*, the gradient of water vapor density was set as driving force of diffusion (equation (9)). Consistently with the coating, mass transfers were set to zero on these opposite sides.

$$J_w=-\frac{D_v}{\mu(RH)}\cdot\frac{\partial\rho_v}{\partial x} \quad (9)$$

With J_w, the moisture flux density (kg·m^{-2}·s^{-1}), ρ_v the water vapor density (kg·m^{-3}), D_V the coefficient diffusion of water vapor in air (m^2·s^{-1}), μ the water vapor diffusion resistance factor of the material. μ depend on relative humidity (RH) according to the expression given by [39].

3 Results and discussion

3.1 General trends

Figure 5 shows the evolution of the moisture content of the cylinder c_1 located in the centre of the sample during the three–months experiment. The temperature boundary conditions at the sample ends were added in the graph to localise the three phases of the thermal sequence. Following the first temperature change on the opposite sides of the sample (phase 1), an increase in moisture content is visible on the cold side. During the first days of phase 1, the measured temperature varies between 15 and 20°C, despite a set point maintained at 20°C, resulting in relatively large moisture content variations closest to the cold zone. This regulation problem was due to water condensation on the Peltier module, which disturbed its operation. Then, a phase of return to isothermal conditions on both sides of the sample was applied for a period of 15 days. During this second phase, the moisture content profile equilibrates over the height of the sample. Finally, during the last phase of the thermal loads, between day 45 and day 60, an increase in moisture content on the cold side, alternatively at the top or bottom of the sample, is clearly visible in connection with the cyclic temperature oscillations. These phases are descried in detail hereafter.

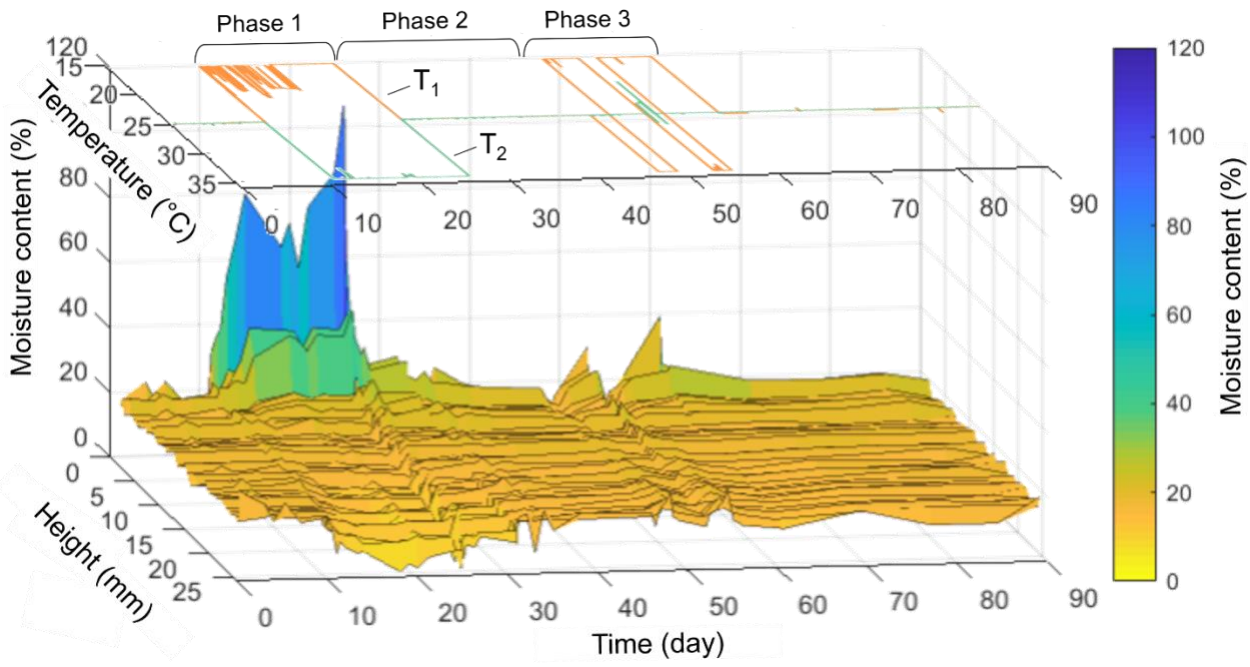

Figure 5: Evolution of the moisture content field in the central cylinder c_1, together with the actual temperature imposed at the two faces at z = 0 mm (orange curve) and z = 25 mm (green curve).

3.2 Phase 1: Non-isothermal conditions

Phase 1 corresponds to the application of a constant temperature gap of 20°C between the two opposite sides of the sample for 15 days. Initially at a temperature of 25°C, the top and bottom sides

were subjected to temperatures of 15°C (T_1) and 35°C (T_2) respectively. The temporal evolution of the moisture content along c_1 – the central cylinder of the sample – is shown in Figure 6, from both the experimental data (solid lines) and simulated data (dotted lines).

The experimental results indicate an increase in moisture content in the ROIs located near the cold surface (T_1 = 15°C). Conversely, moisture near the warm surface (T_2 = 35°C) decreases. The temperature gradient induces by the changes in boundary conditions perturbates the equilibrium between the relative humidity and the water activity defined by the moisture sorption isotherm of wood. This difference is quickly compensated at each point by a change in the partial vapor pressure (by adsorption or desorption), which led to a gradient in the partial vapor pressure of water and thus to a diffusion of moisture from the warm side to the cold side. As all faces of the sample are impervious, the average moisture content remained constant over time. The development of a temperature gradient therefore led to a redistribution of moisture until a new, dynamic, thermodynamic equilibrium was reached. At steady-state, the moisture content profile is constant because the temperature gradient and the moisture content gradient act in opposite directions:

- Water vapor migrates from hot zones to cold zones by thermo-diffusion,
- Bound water and liquid water migrate from zone with high moisture content to zone with low moisture content by diffusion and capillary migration respectively.

It is important to mention that, by using the gradient of water vapor density as driving force for mass diffusion, *TransPore* was able to capture the trends of the moisture experimental profiles over time. This means that the gradient of water vapor density is able to capture, in one single driving force, the combined effects of temperature and moisture content gradients.

Another interesting effect can be seen on the cold side, where the moisture content is higher than the fibre saturation point (near 29% of moisture content, dry basis for this temperature level according to [1]. Indeed, both experimental and simulated data suggested the presence of free water within the ROIs #EW 51, #TW 50 and #LW 50. In this part of the sample, the moisture content was not uniform and its spatial variation was not monotonic. These local variations above X_{fsp} were explained by a density variation of 3 to 4 times within the rings between earlywood (EW) and latewood (LW) of Norway spruce. Therefore, the capillary water storage capacity is higher in EW due to a higher fraction of lumens than in LW while the capillary pressure is larger in latewood due to smaller lumens [40–42].

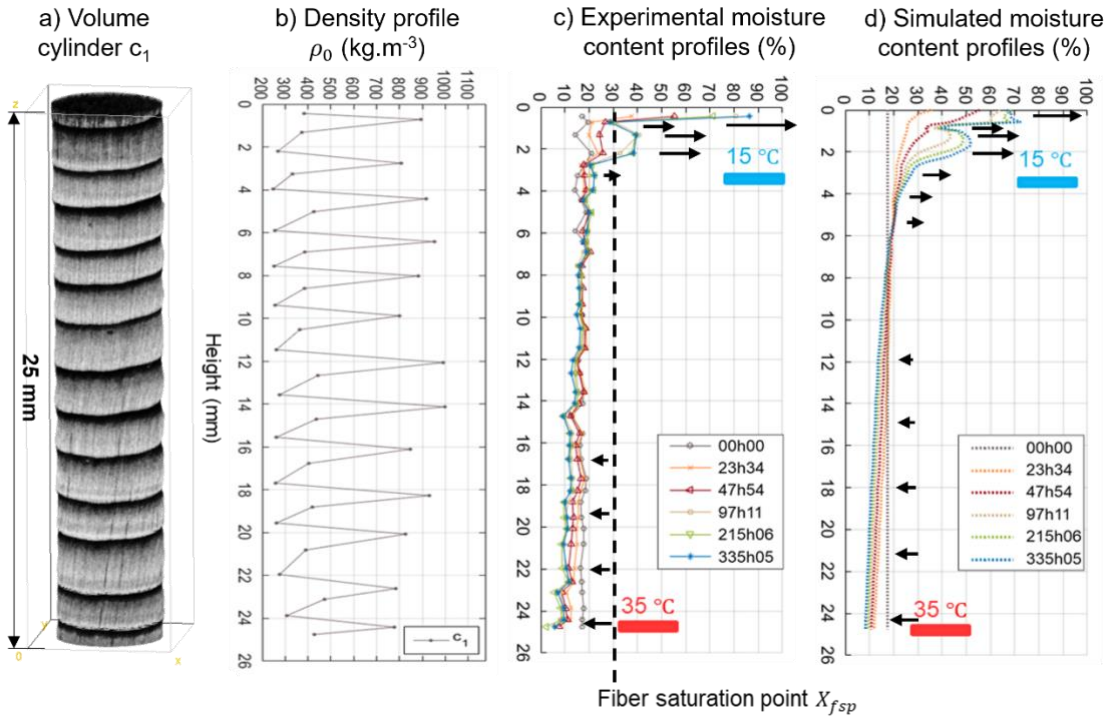

Figure 6: Evolution of the moisture content profile over time of c_1 – central cylinder – as a function of height under non-isothermal conditions (phase 1); a) volume cylinder c_1, b) density profile ($kg{\cdot}m^{-3}$), c) Experimental moisture content profiles (%) and d) Simulated moisture content profiles (%)

To visualise the distribution of water within the cells in more detail, axial cross-sections of the sample, in the R-T and R-L planes of wood are presented in Figure 7a and Figure 7b.

The $CT_{numbers}$ are presented in an inverted grey scale to ease the observation: dark grey areas have a higher density than light grey regions. Two vertical dotted lines were added to the sides of the sections to mark the dimensional variations of the sample over time. The sample diameter along its tangential direction increased near the cold plate and decreased near the hot plate. This is a consequence of shrinkage-swelling which follows the variation in bound water content. The sample diameter along the longitudinal direction of the wood is stable due to the negligible longitudinal shrinkage coefficient in this direction. In these axial sections, it is possible to observe the appearance of black spots, due to the presence of free water, at the top of the sample during phase 1 (Figure 7a.2-3 and Figure 7b.2-3). According to Figure 7a (R-T section), the location of the free water was heterogeneous within the rings and appeared to migrate locally in the radial direction forming water columns (pink arrows). This observation was particularly marked in the radial resin canals (Figure 7a3). In contrast, as observed in the R-L sections (Figure 7b), water did not migrate from tracheid to tracheid. These free water migrations in the pore network are in perfect agreement with direct observation of liquid water flow into Norway spruce sample using high resolution X-ray CT during imbibition [43].

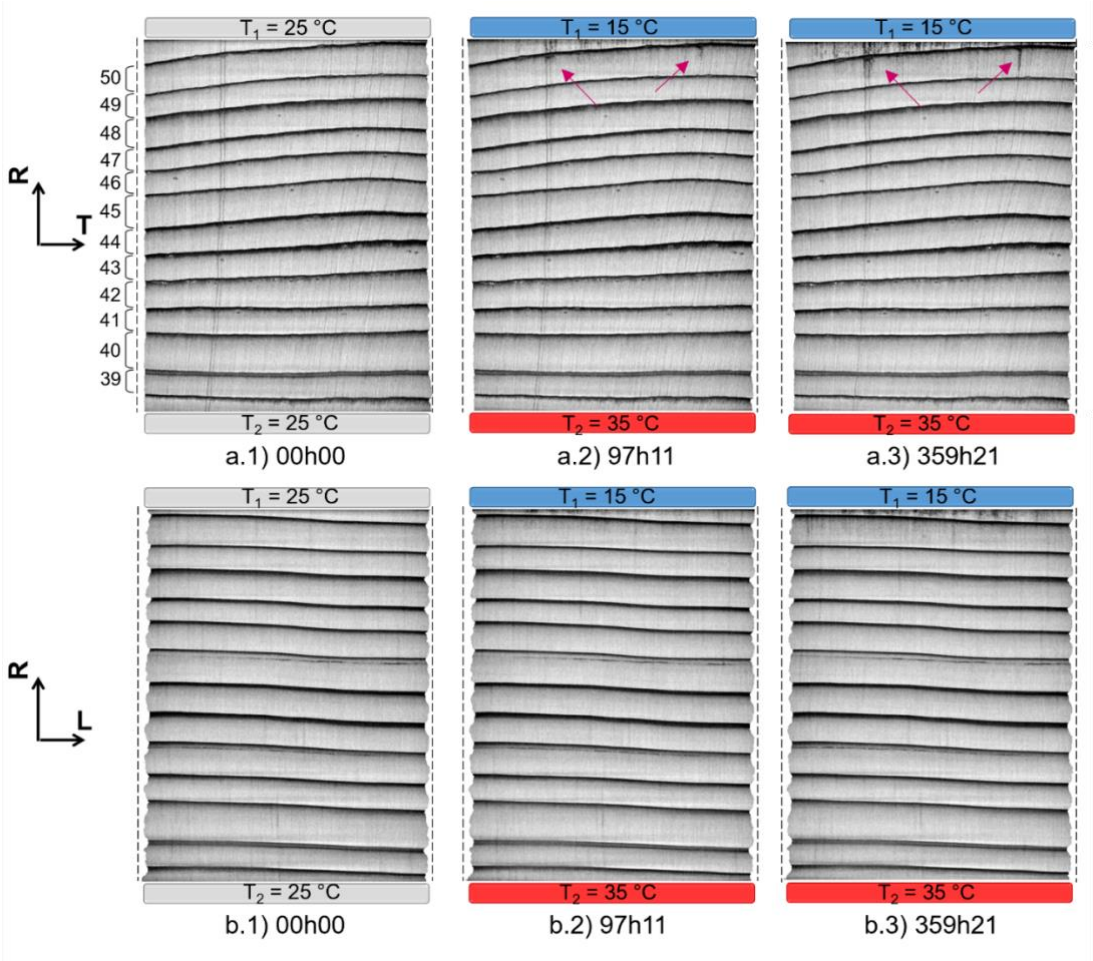

Figure 7: Tomographic sections through the axis of the sample during phase 1 a) in the R-T plane and b) in the R-L plane. The dark grey level is equivalent to the denser material than the light grey level

These moisture content profiles confirmed what was suggested – but was not accessible – in the work [21] which used X-ray radiography to follow the evolution of the moisture content field in a wood sample under non-isothermal conditions. These results showed the same trends in the evolution of the moisture profile but without local variations, explained by the choice of diffuse pore hardwood species (*Sorbus terminalis*) known to be very homogeneous. At the end of their experiment, the measured moisture content was around 40% near the cold plate side, hence above X_{fsp}.

During isothermal phase 2, an expected redistribution of moisture was observed within the sample (Figure 5). For this reason, the following section relate more specifically the phase 3.

3.3 Phase 3: Dynamic conditions

Phase 3 corresponds to the establishment of dynamic conditions consisting of two cycles. One side of the sample (x = 0 mm) was subjected to a temperature T_1 15°C and then 35°C while, on the other side (x = 25 mm), the temperature T_2 was maintained at 25°C (Table 2).

Table 2 : Setpoint temperature for each semi-cycles and their duration

	Cycle 1		Cycle 2	
	Semi-cycle 1.1	**Semi-cycle 1.2**	**Semi-cycle 2.1**	**Semi-cycle 2.2**
Temperature T_1 (x = 0 mm)	35°C	15°C	35°C	15°C
Temperature T_2 (x = 25 mm)	25°C	25°C	25°C	25°C
Duration (h)	49.6	96	48.8	145.8

Figure 8 shows the evolution of the moisture profile, for cylinder c_1, following the change of the imposed temperatures for each semi-cycle (Table 2). Despite the noise in the experimental moisture content values, it is clear that the moisture content varies after each change of conditions, significantly at the side submitted to temperature variations, but also at the opposite side maintained at constant temperature. The perturbed depth of the sample increase with the duration of the cycle. The longer duration of the 1.2 and 2.2 semi-cycles led to a higher accumulation of moisture at the cold side (T_1 = 15°C), with values approaching or exceeding X_{fsp}. The variation in moisture content reached a maximum of 35% (#EW 51) whereas it did not exceed 13% on the opposite side (T_2 = 25°C). Consistently, the amplitude of these variations from one semi-cycle to the other decreases with the distance of the ROI to the end of the sample. Thus, in the middle of the sample, few variations are observed. A reversal of the moisture profiles therefore took place in the sample with the possibility of observing an increase in local moisture content following the change in temperature T_1 from 15 to 35°C. This moisture migration is highlighted by the green arrows in Figure 8 – 2.1 (at time 6h20min) in comparison with the moisture content profile in Figure 8 – 1.2 (at time 95h14min).

The moisture profile trends were correctly predicted by *TransPore* where the alternation of the moisture profiles was reproduced across cycles. It should be noted that the model predicts moisture variations over the entire height of the sample. Consequently, in the semi-cycles 1.2 and 2.2, the initial moisture content at 25 mm is higher that the experimental one. In turn, the inversion of the moisture content profiles is delayed on the experimental profiles. Lateral heat losses in the experiment could be sufficient to reduce the temperature gradient in the middle of the sample, and therefore to exacerbate the moisture variations at the sample ends. Similarly, these thermal losses are proportional to the temperature gap between the sample temperature and the ambient temperature (T = 25°C). Furthermore, the model used a unique sorption function relating moisture content to relative humidity that did not take into account the sorption hysteresis expressed under cyclic conditions [44–46]. These discrepancies between measurements and simulations point out the limitations of both the 1D formulation and the ability to measure an absolute local moisture content using CT imaging. Still the

trends are good and the gradient of vapor pressure as synthetic driving force in non-isothermal conditions is confirmed.

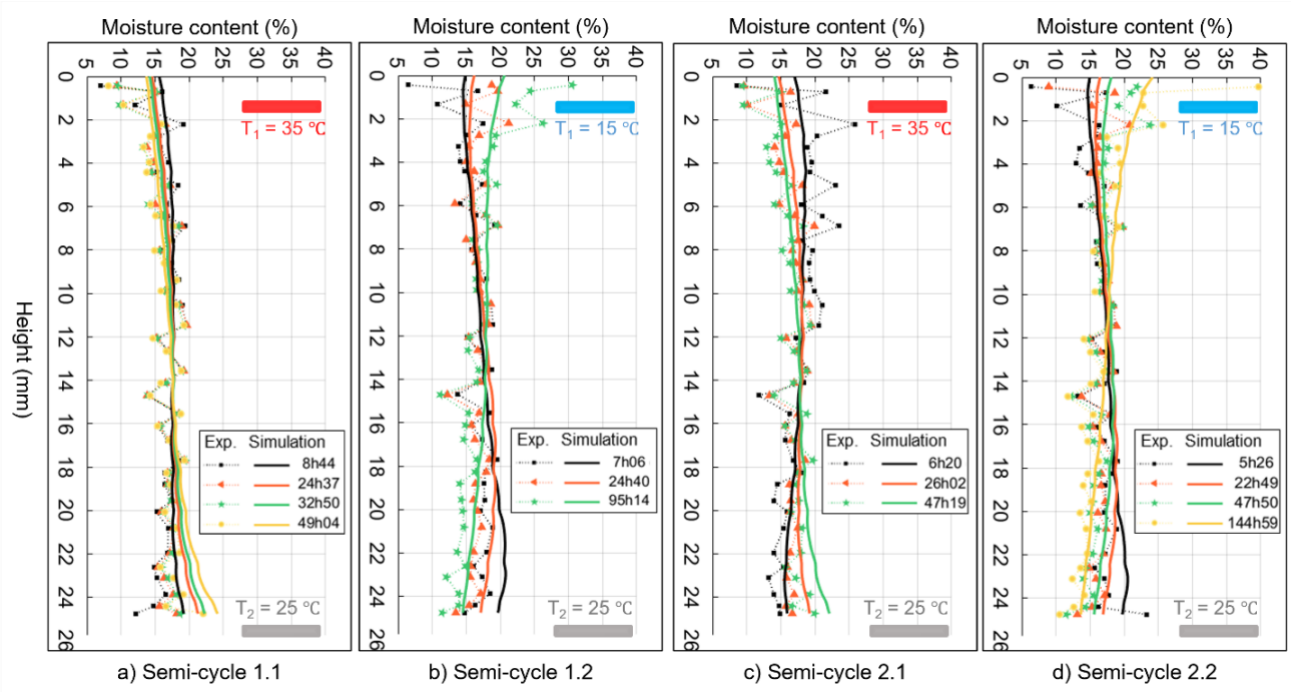

Figure 8: Evolution of moisture content profiles over time of the ROI c_1 – central cylinder – under dynamic conditions (phase 3)

4 Conclusion and perspectives

Moisture migration within a Norway spruce sample in the presence of a thermal gradient was investigated by CT scanning. This technique required the design of an original experimental setup to set and maintain accurate boundary conditions including during X-ray imaging. The conversion of the $CT_{numbers}$ into moisture content in the sample – discretized into regions of interest – gave access to the spatio-temporal evolution of the moisture content field following three phases of thermal solicitations. The results obtained during the three months of experiments were compared with the heterogeneous *TransPore* model to draw the following conclusions:

- Under non-isothermal conditions, the monitoring of moisture profiles allows the migration of moisture from the hot side to the cold side, to be quantified,
- The observed moisture content field showed strong local variations along the sample due to the temperature gradient when X_{fsp} was reached. These variations were related to the effect of the heterogeneous density of Norway spruce within rings on capillary water,

- The computational model *TransPore* 1D allowed all trends to be nicely reproduced using the gradient of water vapor density as unique, "synthetic", driving force in these non-isothermal conditions.

However, some discrepancies remained in the predicted/measured moisture fields under dynamic thermal conditions (characteristic of the off-season) and under stationary non-isothermal conditions (corresponding to a winter configuration within a wall). This is partly explained by lateral thermal losses in the experiment and by the neglected effect of history in the model (sorption hysteresis) or the account for local wood properties (capillary pressure, difference in pit aspiration between earlywood and latewood). These points pave the route for further investigation.

Appendix

Calibration of Moisture Content

The values of constants A and B involved in equation (8) must be calibrated. This was done thanks to the initial state, when the moisture content was uniform throughout the sample:

$$\frac{\rho_0(ROI)}{1+\epsilon_v\big(X(t=0)\big)}\cdot\big(1+X(t=0)\big)=A\cdot GsV^*(ROI,t=0)+B(c_i) \quad (10)$$

This equation was applicable to each of the ROIs. In this model, the unknowns were: the value of A, four values of B (i.e. one for each cylinder c_i) and 39 values of ρ_0 corresponding to each ROI. The values of ρ_0, A and B were related by a linear function. Thus, solving this system of equations alone would generate an infinite number of solutions, each one multiple of the others. To identify a unique set of values, it was necessary to add two constraints: (i) initially (when the moisture content was assumed to be uniform within the sample), the average density of the ROIs weighted by their respective volumes was equal to the density of the sample (equation (11) and (ii) the average of the anhydrous density of all ROIs located in earlywood by their respective anhydrous volumes obtained by 3D imaging was equal to that obtained in 2D imaging using a twin sample in [33] (equation (12)). The earlywood region was chosen because of its larger size than the latewood region and its significant difference in density compared to the average density of the sample.

$$\rho_{sample}(t=0)=\frac{\sum_{ROI}\rho(ROI,t=0)\cdot V_{voxel}\cdot N_{voxels}(ROI,t=0)}{\sum_{ROI}V_{voxel}\cdot N_{voxels}(ROI,t=0)}=\frac{\frac{1+X(t=0)}{1+\epsilon_v\big(X(t=0)\big)}\cdot\sum_{ROI}\rho(ROI,t=0)\cdot V_{voxel}\cdot N_{voxels}(ROI,t=0)}{\sum_{ROI}N_{voxels}(ROI,t=0)} \quad (11)$$

with N_{voxels} the number of voxel and V_{voxel} the volume of each voxel.

	$$\frac{\sum_{ROI_{EW,2D}}^{39to50} \rho_0(ROI_{EW\ 2D}) \cdot N_{pixels}(ROI_{EW\ 2D})}{\sum_{ROI_{EW,2D}}^{39to50} N_{pixels}(ROI_{EW\ 2D})} = \frac{\sum_{ROI_{EW,3D}}^{39to50} \rho_0(ROI_{EW\ 3D}) \cdot N_{voxels}\left(ROI_{EW\ 3D}(t=0)\right)}{\sum_{ROI_{EW,3D}}^{39to50} N_{voxels}\left(ROI_{EW\ 3D}(t=0)\right)}$$	(12)

The numerical solution of equations (10), (11) and (12) identified the constants values of the model (8) summarised in Table 3 and the anhydrous densities plotted as a function of the sample height in Figure 4.

Table 3: Coefficient values of A and B

A	**B**			
	c_1	c_2	c_3	c_4
$4.6566 \cdot 10^4$	$4.6763 \cdot 10^{-4}$	$4.6770 \cdot 10^{-4}$	$4.6788 \cdot 10^{-4}$	$4.6844 \cdot 10^{-4}$

Acknowledgements

Communauté urbaine du Grand Reims, Département de la Marne, Région Grand Est and European Union (FEDER Champagne-Ardenne 2014-2020) are acknowledged for their financial support to the Chair of Biotechnology of CentraleSupélec and the Centre Européen de Biotechnologie et de Bioéconomie (CEBB).

For four years (from 05/01/2016 to 07/31/2020) and with a total budget of 965,000 €, 3D-BioMat has been co-financed by the Grand Reims (31%) and the European Union (48.7%—i.e., 50% of eligible expenditures). Europe is committed to the Grand Est with the European Regional Development Fund.

ADEME was a partner of the project and co-financed a thesis scholarship within the framework of the theme "sustainable cities and territories," contributing to the development of high-performance buildings integrating bio-sourced materials.

The authors sincerely thank the team of La Fabrique in CentraleSupélec, and more particularly Hanane Meliani and Frédéric Lesage for their availability and advice, as well as Sebastien Gauthier and Mahamadou Mounkaila for their involvement in the fabrication of the experimental setup.

References

[1] J.F. Siau, Transport Process in Wood, Springer-Verlag, Berlin, 1984.

[2] C. Skaar, Wood-Water Relations, Springer Berlin Heidelberg, Berlin, Heidelberg, 1988. https://doi.org/10.1007/978-3-642-73683-4.

[3] S. Hameury, T. Lundström, Contribution of indoor exposed massive wood to a good indoor climate: in situ measurement campaign, Energy Build. 36 (2004) 281–292. https://doi.org/10.1016/j.enbuild.2003.12.003.

[4] O.F. Osanyintola, C.J. Simonson, Moisture buffering capacity of hygroscopic building materials: Experimental facilities and energy impact, Energy Build. 38 (2006) 1270–1282. https://doi.org/10.1016/j.enbuild.2006.03.026.

[5] A. Piot, M. Woloszyn, J. Brau, C. Abele, Experimental wooden frame house for the validation of whole building heat and moisture transfer numerical models, Energy Build. 43 (2011) 1322–1328. https://doi.org/10.1016/j.enbuild.2011.01.008.

[6] H.M. Rafidiarison, Etudes expérimentales des transferts de masse et de chaleur dans les parois des constructions en bois, en vue de leur modélisation. Applications aux économies d'énergie et au confort dans l'habitat, Université de Lorraine, 2012.

[7] V. Cascione, D. Maskell, A. Shea, P. Walker, A review of moisture buffering capacity: From laboratory testing to full-scale measurement, Constr. Build. Mater. 200 (2019) 333–343. https://doi.org/10.1016/j.conbuildmat.2018.12.094.

[8] T. Busser, M. Pailha, A. Piot, M. Woloszyn, Simultaneous hygrothermal performance assessment of an air volume and surrounding highly hygroscopic walls, Build. Environ. 148 (2019) 677–688. https://doi.org/10.1016/j.buildenv.2018.11.031.

[9] E. Latif, R.M.H. Lawrence, A.D. Shea, P. Walker, An experimental investigation into the comparative hygrothermal performance of wall panels incorporating wood fibre, mineral wool and hemp-lime, Energy Build. 165 (2018) 76–91. https://doi.org/10.1016/j.enbuild.2018.01.028.

[10] H. Rafidiarison, R. Rémond, E. Mougel, Dataset for validating 1-D heat and mass transfer models within building walls with hygroscopic materials, Build. Environ. 89 (2015) 356–368. https://doi.org/10.1016/j.buildenv.2015.03.008.

[11] T. Busser, J. Berger, A. Piot, M. Pailha, M. Woloszyn, Comparison of model numerical predictions of heat and moisture transfer in porous media with experimental observations at material and wall scales: An analysis of recent trends, Dry. Technol. 37 (2019) 1363–1395. https://doi.org/10.1080/07373937.2018.1502195.

[12] P. Perré, A. Challansonnex, J. Colin, On the importance of heat and mass transfer coupling for the characterization of hygroscopic insulation materials, Int. J. Heat Mass Transf. 133 (2019) 968–975. https://doi.org/10.1016/j.ijheatmasstransfer.2018.12.105.

[13] S. Avramidis, N. Kuroda, J.F. Siau, Experiments in Nonisothermal Diffusion of Moisture in Wood. Part II., Wood Fiber Sci. (1987) 407–413.

[14] St. Avramidis, J.F. Siau, Experiments in nonisothermal diffusion of moisture in wood. Part III., Wood Sci. Technol. 21 (1987) 329–334. https://doi.org/10.1007/BF00380200.

[15] R. Peuhkuri, C. Rode, K.K. Hansen, Non-isothermal moisture transport through insulation materials, Build. Environ. 43 (2008) 811–822. https://doi.org/10.1016/j.buildenv.2007.01.021.

[16] J.F. Siau, F. Bao, S. Avramidis, Experiments in Nonisothermal Diffusion of Moisture in Wood, Wood Fiber Sci. (1986) 84–89.

[17] J.F. Siau, M. Babiak, Experiments on Nonisothermal Moisture Movement in Wood, Wood Fiber Sci. (1983) 40–46.

[18] L. Hansson, E. Cherepanova, Determination of wood moisture properties using a CT-scanner in a controlled low-temperature environment, Wood Mater. Sci. Eng. 7 (2012) 87–92. https://doi.org/10.1080/17480272.2012.662701.

[19] M.S. Gilani, P. Vontobel, E. Lehmann, J. Carmeliet, D. Derome, Moisture Migration in Wood Under Heating Measured by Thermal Neutron Radiography, Exp. Heat Transf. 27 (2014) 160–179. https://doi.org/10.1080/08916152.2012.757677.

[20] T. Arends, A.J. Barakat, L. Pel, Moisture transport in pine wood during one-sided heating studied by NMR, Exp. Therm. Fluid Sci. 99 (2018) 259–271. https://doi.org/10.1016/j.expthermflusci.2018.08.004.

[21] A. Bouali, R. Rémond, G. Almeida, P. Perré, Thermo-diffusion in wood: X-ray MC profiles analysed using a 2-D computational model, in: In Proceedings of the 18 th International Drying Symposium, Xiamen, 2012.

[22] M.H. Ramage, H. Burridge, M. Busse-Wicher, G. Fereday, T. Reynolds, D.U. Shah, G. Wu, L. Yu, P. Fleming, D. Densley-Tingley, J. Allwood, P. Dupree, P.F. Linden, O. Scherman, The wood from the trees: The use of timber in construction, Renew. Sustain. Energy Rev. 68 (2017) 333–359. https://doi.org/10.1016/j.rser.2016.09.107.

[23] Martin, Dynamique des transferts d'humidité au sein de l'épicéa commun (Picea abies (L.) Karst.): mesures par imagerie X et simulations numériques, Thesis, Université de Lorraine, 2022.

[24] Grangeat P, La tomographie : fondements mathématiques, imagerie microscopique et imagerie industrielle, Lavoisier Hermès Science publ, 2002.

[25] A.C. Kak, M. Slaney, Principles of computerized tomographic imaging, Society for Industrial and Applied Mathematics, Philadelphia, 2001.

[26] S. Seltzer, XCOM-Photon Cross Sections Database, NIST Standard Reference Database 8, (1987). https://doi.org/10.18434/T48G6X.

[27] O. Lindgren, Medical CT-Scanners for Non-Destructive Wood Density and Moisture Content Measurements, Thesis, Luleå University of Technology - LTU, 1992.

[28] O. Lindgren, J. Davis, P. Wells, P. Shadbolt, Non-destructive wood density distribution measurements using computed tomography, Holz Als Roh- Werkst. 50 (1992) 295–299. https://doi.org/10.1007/BF02615356.

[29] C. Freyburger, F. Longuetaud, F. Mothe, T. Constant, J.-M. Leban, Measuring wood density by means of X-ray computer tomography, Ann. For. Sci. 66 (2009) 804–804. https://doi.org/10.1051/forest/2009071.

[30] J. Skog, Sapwood Moisture Content Measurements in Scots Pine Sawlogs Combining X-ray and 3D Scanning, Thesis, Luleå University of Technology - LTU, 2009.

[31] P. Jacquin, F. Mothe, F. Longuetaud, A. Billard, B. Kerfriden, J.-M. Leban, CarDen: A software for fast measurement of wood density on increment cores by CT scanning, Comput. Electron. Agric. 156 (2019) 606–617. https://doi.org/10.1016/j.compag.2018.12.008.

[32] R. Baettig, R. Rémond, P. Perré, Measuring moisture content profiles in a board during drying: a polychromatic X-ray system interfaced with a vacuum/pressure laboratory kiln, Wood Sci. Technol. 40 (2006) 261–274. https://doi.org/10.1007/s00226-006-0068-7.

[33] B. Martin, J. Colin, P. Lu, M. Mounkaila, J. Casalinho, P. Perré, R. Rémond, Monitoring imbibition dynamics at tissue level in Norway spruce using X-ray imaging, Holzforschung. 75 (2021) 1081–1096. https://doi.org/10.1515/hf-2020-0269.

[34] P. Perré, H. Huber, Measurement of free shrinkage at the tissue level using an optical microscope with an immersion objective: results obtained for Douglas fir (Pseudotsuga menziesii) and spruce (Picea abies), Ann. For. Sci. 64 (2007) 255–265. https://doi.org/10.1051/forest:2007003.

[35] P. Perré, Le séchage convectif de bois resineux : choix, validation et utilisation d'un modèle, These de doctorat, Paris, 1987.

[36] P. Perré, A. Degiovanni, Simulation par volumes finis des transferts couplés en milieux poreux anisotropes: séchage du bois à basse et à haute température, Int. J. Heat Mass Transf. 33 (1990) 2463–2478. https://doi.org/10.1016/0017-9310(90)90004-E.

[37] P. Perré, I.W. Turner, A 3-D version of TransPore: a comprehensive heat and mass transfer computational model for simulating the drying of porous media, Int. J. Heat Mass Transf. 42 (1999) 4501–4521. https://doi.org/10.1016/S0017-9310(99)00098-8.

[38] G.A. Spolek, O.A. Plumb, Capillary pressure in softwoods, Wood Sci. Technol. 15 (1981) 189–199. https://doi.org/10.1007/BF00353471.

[39] X. Zhang, H.M. Künzel, W. Zillig, C. Mitterer, X. Zhang, A Fickian model for temperature-dependent sorption hysteresis in hygrothermal modeling of wood materials, Int. J. Heat Mass Transf. 100 (2016) 58–64. https://doi.org/10.1016/j.ijheatmasstransfer.2016.04.057.

[40] B.G. Butterfield, B.A. Meylan, Three-dimensional structure of wood; an ultrastructural approach, Springer Netherlands, Dordrecht, 1980. https://doi.org/10.1007/978-94-011-8146-4_1.

[41] K. Wilson, D.J.B. White, The anatomy of wood: its diversity and variability., Stobart & Son Ltd., London, 1986.

[42] P. Perré, I.W. Turner, Determination of the Material Property Variations Across the Growth Ring of Softwood for Use in a Heterogeneous Drying Model Part 1. Capillary Pressure,Tracheid Model and Absolute Permeability, Holzforschung. 55 (2001) 318–323. https://doi.org/10.1515/HF.2001.052.

[43] B. Martin, J. Colin, P. Perré, J. Casalinho, M. Mounkaila, P. Lu, R. Rémond, CT investigation of 3D liquid pathways in the anatomical structure of Norway spruce wood during imbibition, Holzforschung. 76 (2022) 592–603. https://doi.org/10.1515/hf-2021-0154.

[44] J.G. Downes, B.H. Mackay, Sorption kinetics of water vapor in wool fibers, J. Polym. Sci. 28 (1958) 45–67. https://doi.org/10.1002/pol.1958.1202811605.

[45] A. Patera, D. Derome, M. Griffa, J. Carmeliet, Hysteresis in swelling and in sorption of wood tissue, J. Struct. Biol. 182 (2013) 226–234. https://doi.org/10.1016/j.jsb.2013.03.003.

[46] G. Almeida, R. Rémond, P. Perré, Hygroscopic behaviour of lignocellulosic materials: Dataset at oscillating relative humidity variations, J. Build. Eng. 19 (2018) 320–333. https://doi.org/10.1016/j.jobe.2018.05.005.